Fall 12-2017

Condensation and subsequent freezing delays as a result of using a femtosecond laser functionalized surface

Chongji Huang
University of Nebraska-Lincoln, chongjihuang@icloud.com

CONDENSATION AND SUBSEQUENT FREEZING DELAYS

AS A RESULT OF USING A

FEMTOSECOND LASER FUNCTIONALIZED SURFACE

by

Chongji Huang

A THESIS

Presented to the Faculty of

The Graduate College at the University of Nebraska

In Partial Fulfillment of Requirements

For the Degree of Master of Science

Major: Electrical Engineering

Under the Supervision of Professor Dennis R. Alexander

Lincoln, Nebraska

December, 2017

CONDENSATION AND SUBSEQUENT FREEZING DELAYS

AS A RESULT OF USING A

FEMTOSECOND LASER FUNCTIONALIZED SURFACE

Chongji Huang, M.S.

University of Nebraska, 2017

Advisor: Dennis R. Alexander

Femtosecond laser surface processing (FLSP) enhances the anti-icing properties of a commonly used aircraft alloy, Al 7075-O Clad. The wettability of Al 7075-O Clad was altered by changing the surface morphology through FLSP and the surface chemistry through siloxane vapor deposition. Tall mound and short mound FLSP functionalized surfaces were created through two sets of laser parameters. Atmospheric condensation and subsequent freezing of condensates on FLSP Al 7075-O Clad was studied. Results indicate that both structure height and surface wettability play a role in the delay of freezing. Freezing occurred on the FLSP superhydrophilic surface faster than on a unprocessed Al 7075-O Clad surface; however, freezing was delayed for all superhydrophobic FLSP surfaces. Tall structure FLSP functionalized surfaces delayed freezing time longer than short structure FLSP functionalized surfaces, although all were superhydrophobic. FLSP functionalized surfaces were able to delay freezing by up to 530 seconds compared to unprocessed Al 7075-O Clad surfaces. Self-propelled condensate jumping on FLSP functionalized superhydrophobic surfaces occurred during the condensing process. The self-propelled jumping phenomena provides a means to promote anti-icing materials, especially where jumping drops can be swept away in the flowing airstream.

Acknowledgements

I would like to thank my advisor, Dr. Dennis Alexander, for all of his help and support from my early research experiences as an undergraduate research assistant through my M.S program. He has truly been an inspiration and has provided the guidance I have needed throughout graduate school. I would also like to thank my committee members, Dr. Natale Ianno and Dr. Ming Han, for all of their help and support.

Thank you to all of the lab mates I have worked with through the years: Ryan Bell, William Conner Thomas, Alfred Tsubaki, and Nick Roth. Also, I would like to thank Dr. Craig A. Zuhlke for all of his help and his guidance in my research career.

Finally, I would like to thank all of my family for their support. Thanks to my parents, Xiaohong Tang and Shifu Huang, for all of their love and support. A special thanks to my girlfriend, Zhexi He, for supporting me over the past eight years.

Grant Information

Table of Contents

List of Figures

List of Tables

Chapter 1

Background

1.1. Introduction

There are many applications where metallic anti-icing surfaces would be desirable. Typical applications include power line cables, aircraft wings, wind turbines, and cold weather marine applications such as guide wires. Various anti-icing studies have been reported previously [1]–[4]. Surface wettability, which can be controlled by micro/nanoscale features, along with surface chemistry, is an important parameter for controlling ice buildup. The water contact angle, is defined as the angle that is measured through water on which the surface is attached by the water droplets as shown in Figure 1. This contact angle is often used to determine surface wettability. Droplets of water (w) on a solid (s) with an interface (w, s) is shown in Figure 1. The contact angle is defined as θ and the corresponding surface energies is defined as γ. This example is schematically shown in Figure 1 [4]. A hydrophobic surface is a surface with a water contact angle greater than 90°. A superhydrophobic surface is a surface with a water contact angle greater than 150°, and a superhydrophilic surface is a surface with a water contact angle equal to 0°. A superhydrophobic surface is often used in anti-icing studies [1]–[4].
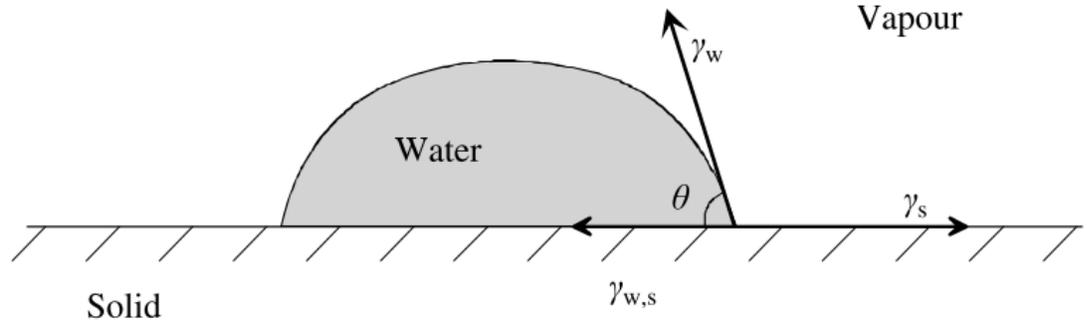
Figure 1. Water droplet on a solid surface and the definition of the contact angle. [4]

For the situation in Figure 1, the Young equation for the equilibrium is shown by

$$\gamma_{W,s} + \gamma_W \cos\theta = \gamma_s \ [4] \tag{1}$$

The ice (i) defined when the droplets are frozen on the solid (s). The situation of water droplets is frozen into ice is shown in Figure 1.

In a work by Makkonen et al., their interest is required to remove the ice in order to achieve anti-icing property, i.e., break the bond between ice and surface, and form two new individual surface (ice and surface) in the absence of deformations [4]. The thermodynamic work of adhesion W_a is defined as

$$W_a = \gamma_s + \gamma_i - \gamma_{i,s}[4] \tag{2}$$

By inserting γ_s from the Young equation (1) into equation (2), the result is shown in equation (3)

$$W_a = \gamma_i + \gamma_W \cos\theta + (\gamma_{W,s} - \gamma_{i,s}) \ [4] \tag{3}$$

In this case, we assume that the surface energies of water and ice are relatively the same [5] and consider that interfacial energies of water and ice at the solid interface are relatively the same too, W_a can be rewritten as

$$W_a \approx \gamma_W(1 + \cos\theta) \ [4] \tag{4}$$

Ideally, we should in ice removal expect a deterministic dependence between the contact angle of the droplets and the work of adhesion, which is shown in Equation (4) and Figure 2 [4].
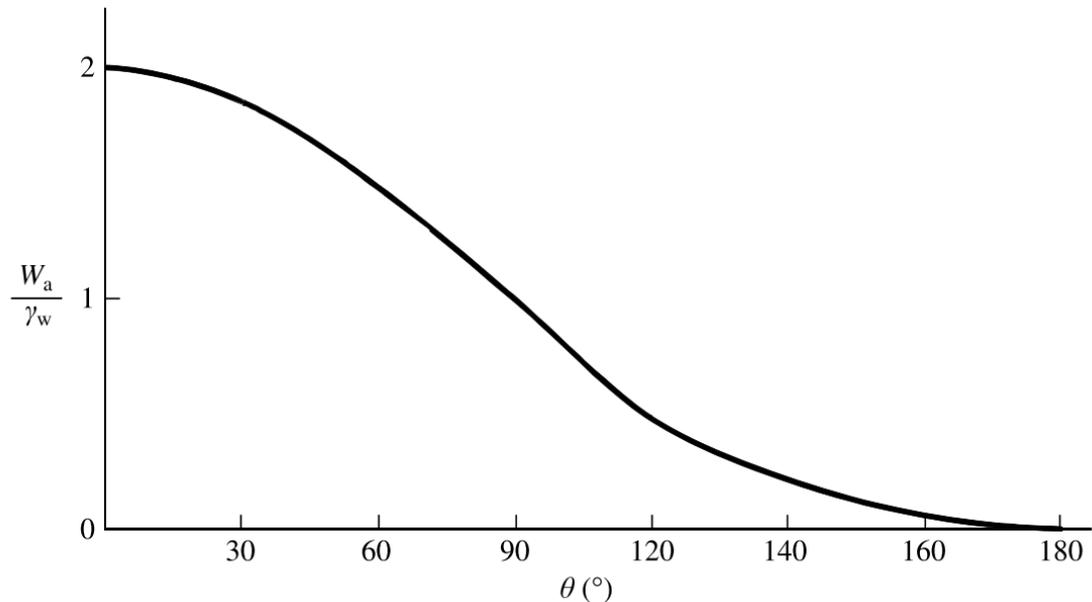
Figure 2. Thermodynamic work of ice adhesion scaled by the surface tension of water as a function of water contact angle θ. [4]

According to Makkonen et al., the water contact angle plays an important role in ice adhesion theoretically [4].

Superhydrophobic and hydrophobic surfaces have been shown to delay freezing on various substrates [1]–[3], [6]–[10]. In a work by Van Dyke et al., the relative humidity of the atmosphere was shown to be an important factor in icing condensation. In addition, relative humidity, surface chemistry, and surface patterning all significantly impact freezing temperature, droplet size and distribution, and the estimated droplet volume at freezing due to the changes in coalescence [10].

In a work by Li et al., large scale comparison between an PDMS/modified Nano-silica coated superhydrophobic insulator and an RTV silicone rubber coated insulator is shown in Figure 3 [11].
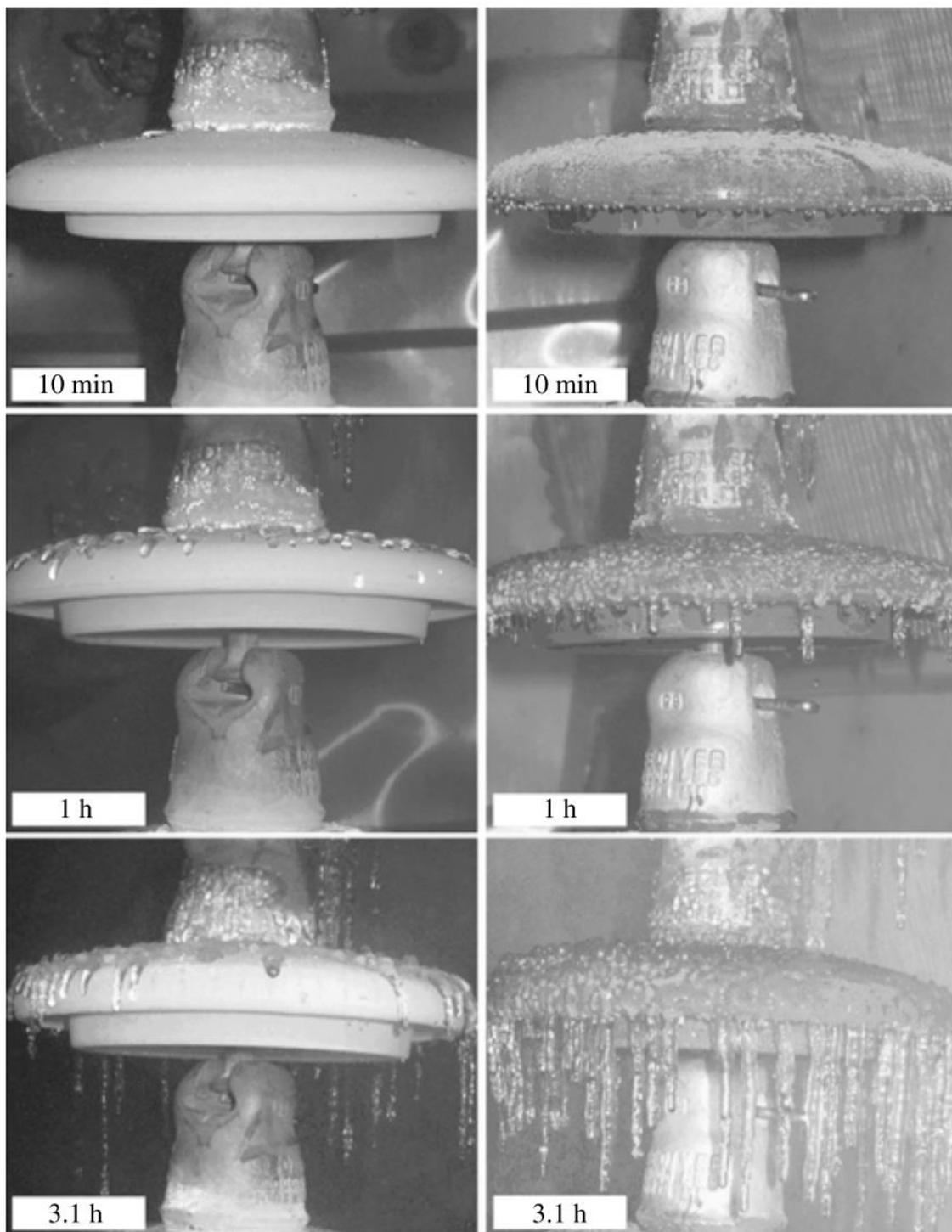
Figure 3. Comparison of ice accumulation on a PDMS/modified Nano-silica coated superhydrophobic insulator (left) and on an RTV silicone rubber coated insulator (right), after different times of laboratory icing test. [11]

The property of anti-icing in this work is determined by the time requirement for the subsequent freezing in the whole monitored area. The time requirement for the subsequent freezing experiment has been shown previously [9], [10].

Femtosecond laser surface processing (FLSP) has previously been shown to produce different self-organized micro/nanoscale surfaces on metals [12]. Structures produced through FLSP can be controlled by varying the laser fluence and pulse count. After FLSP, the FLSP-processed surface is superhydrophilic due to the hydrophilic nature of the Al 7075-O Clad surface. FLSP surfaces can be functionalized and made to be superhydrophobic by vapor deposition. In this work, the delay of condensation and subsequent freezing on superhydrophobic and superhydrophilic FLSP functionalized and unprocessed Al 7075-O Clad surfaces was investigated. Two mound structure surfaces with different structure heights (R_z) were made: a tall mound surface and a short mound surface. The superhydrophobic FLSP functionalized tall mound surfaces experienced the longest time before the condensation froze. Both the hydrophobic tall mound surface and the short mound surface delayed freezing of the condensation for a significant time compared to the unprocessed Al 7075-O Clad surface. The superhydrophilic surface experienced the shortest time until the condensation froze due to the 0° contact angle. The impact of FLSP structures on the time required for freezing of condensation to occur is reported here for the first time.

Condensate on superhydrophobic surfaces has been shown to spontaneously jump upon coalescence [13]. According to Wisdom et al., when the superhydrophobic surface was in the condensation situation of vapor flow, water vapor condensed on the surface and the adhering particles. The interaction of the resulting condensates in liquid form and the

particles on the superhydrophobic surface could cause self-cleaning of the surface. The particle removal process highly depended on the wettability. Depending on their wettability, particles tend to either attach to the air-liquid interface or detach into the bulk fluid. Self-propelled condensates jumping exhibits a self-cleaning effect which has been shown to delay condensation and subsequent freezing time [14]. This work presents self-propelled jumping condensate on FLSP functionalized surfaces.

1.2.   Thesis Organization

Chapter 1 introduces the reader to the background and its organization structure. Chapter 2 describes the equipment and experimental setup used in this work, including sample fabrication, a surface wettability modification system, a contact angle measurement system, a condensate freezing experiment system, and a self-propelled condensates jumping experiment. Chapter 3 presents the results and discussion of the freezing and self-propelled condensates jumping. Chapter 4 includes future work, a summary, and conclusions of the research.

Chapter 2

Experimental Equipment and Procedures

2.1. Sample Fabrication

Quasiperiodic microstructures covered with nanoparticles, were produced through FLSP on various 40 by 40 by 1 mm thick Al 7075-O Clad aircraft aluminum alloy samples. The laser used in this work was a Coherent Astrella laser system, which produces 35 fs, 800 nm pulses at a 1 KHz repetition rate, with a maximum pulse energy of 6 mJ. The size and shape of FLSP micron-scale features were modified by controlling the laser fluence and the number of laser pulses incident on the sample using a technique described by Zuhlke et al. [10], [13]. A diagram of the laser experimental setup is shown in Figure *4*. The Astrella femtosecond laser pulse is guided through a series of optical elements including the shutter, half waveplate, polarizer, mirrors, and 150 mm focal length lens. The sample is placed on the computer-controlled linear stage which can be adjusted in all three dimensions with different moving speeds. The laser pulse is exposed to the sample surface perpendicularly. The laser pulse and the linear stages are controlled by a computer using NI LabVIEW software.
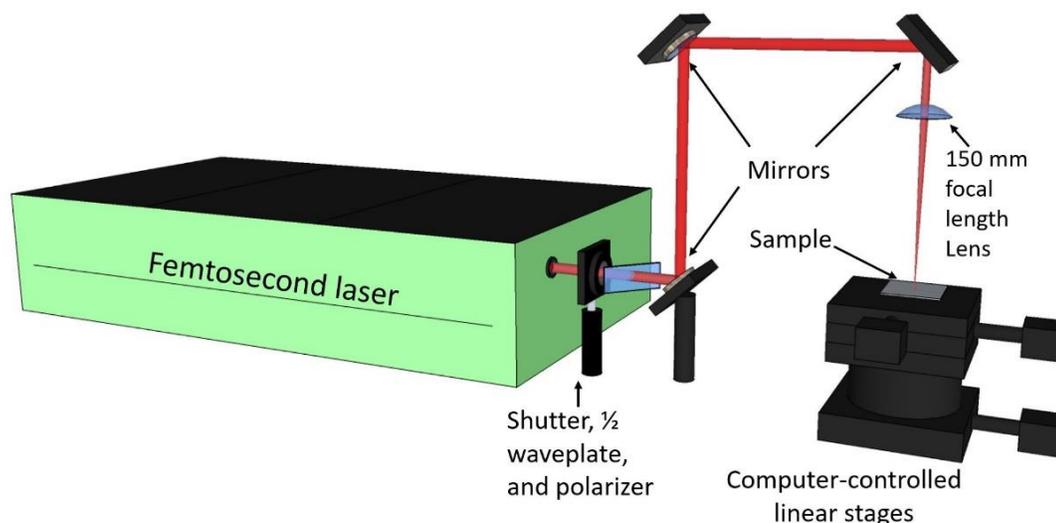
Figure 4. Experimental setup utilized in this work.

By varying the laser fluence, the rastering pitch and the translation speed, two different mound structures were created on Al 7075-O Clad. For tall mound surfaces, the laser fluence value was 6.03 J/cm^2; and the laser spot radius was 200 µm. Thus any single location was irradiated with 341 pulses from the Gaussian pulse with varing energies during the sequence of laser pulses. For the short mound surfaces, the laser fluence value was 2.80 J/cm^2; and the laser spot radius was 282 µm. Each spot on the sample was irradiated with 506 pulses from the Gaussian pulse passing over the surface. Scanning electron microscope (SEM) images were taken using a Philips XL-30 Environmental Scanning Electron Microscope.

2.2.   Surface Wettability Modification and Contact Angle Measurement

The intrinsically superhydrophilic FLSP Al 7075-O Clad surfaces were made superhydrophobic (functionalized) through vapor deposition of VMQ O-rings (McMaster-Carr 9396k105). The surface wettability mesurement system is shown in Figure 5. The

FLSP samples and the O-rings were placed on a Thermolyne® Cimarec® 2 heater and covered with a glass filter funnel. The samples were placed radially around the O-rings. The FLSP surfaces were face up. The air temperature inside the funnel was kept at 182.1 °C, measured by a thermocouple suspended inside the funnel. The heater plate temperature was 263.4 °C, measured with a thermocouple resting on top of the heater plate. The vapor deposition period was 2 hours. For the first 20 minutes, the nozzle of the funnel was left open. After 20 minutes, aluminum foil was used to seal the nozzle. One tall mound surface sample was kept superhydrophilic (referred to as superhydrophilic). All other FLSP samples were made superhydrophobic through vapor deposition of siloxanes (referred to as SMS1, SMS2, TMS1, and TMS2).
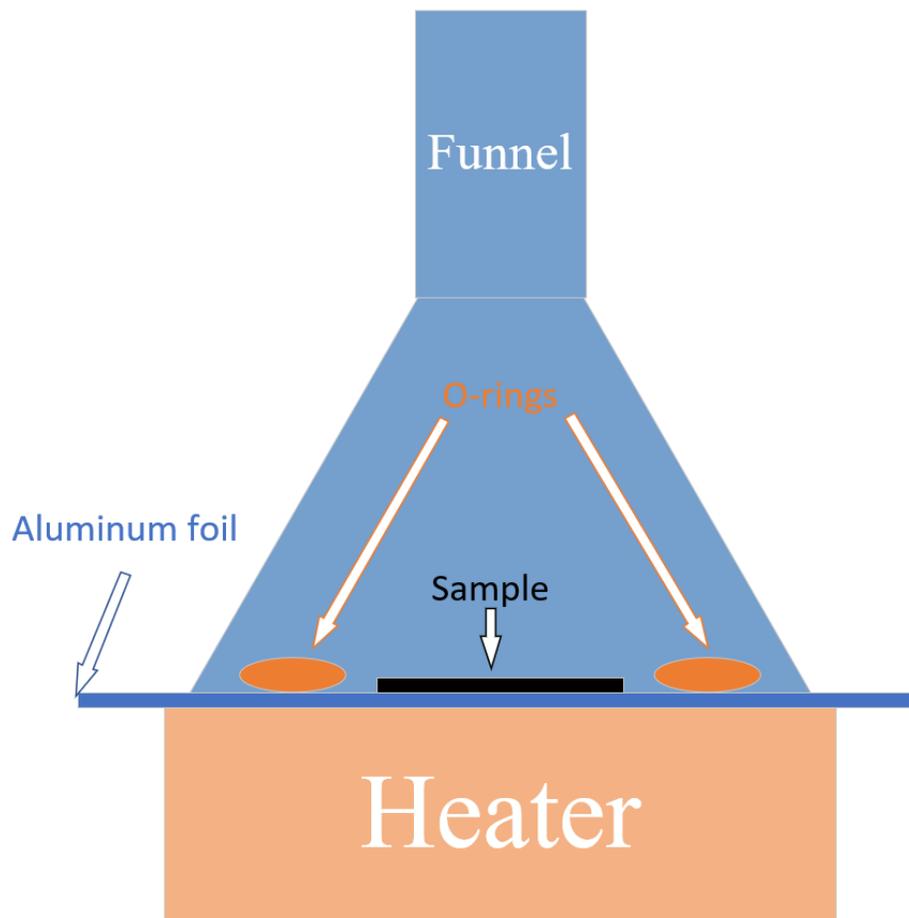
Figure 5. Surface wettability medication system.

The intrinsic contact angle of all samples was measured using a Ramé-hart Goniometer/Tensiometer Model 790. The Ramé-hart Goniometer/Tensiometer system is shown in Figure 6. The water droplet size used for the contact angle measurements was 5 µL. The contact angle of each sample was measured three times using DROPimage Advanced software package, The software automatically measured both the left-side and right-side contact angles 10 times for each run.
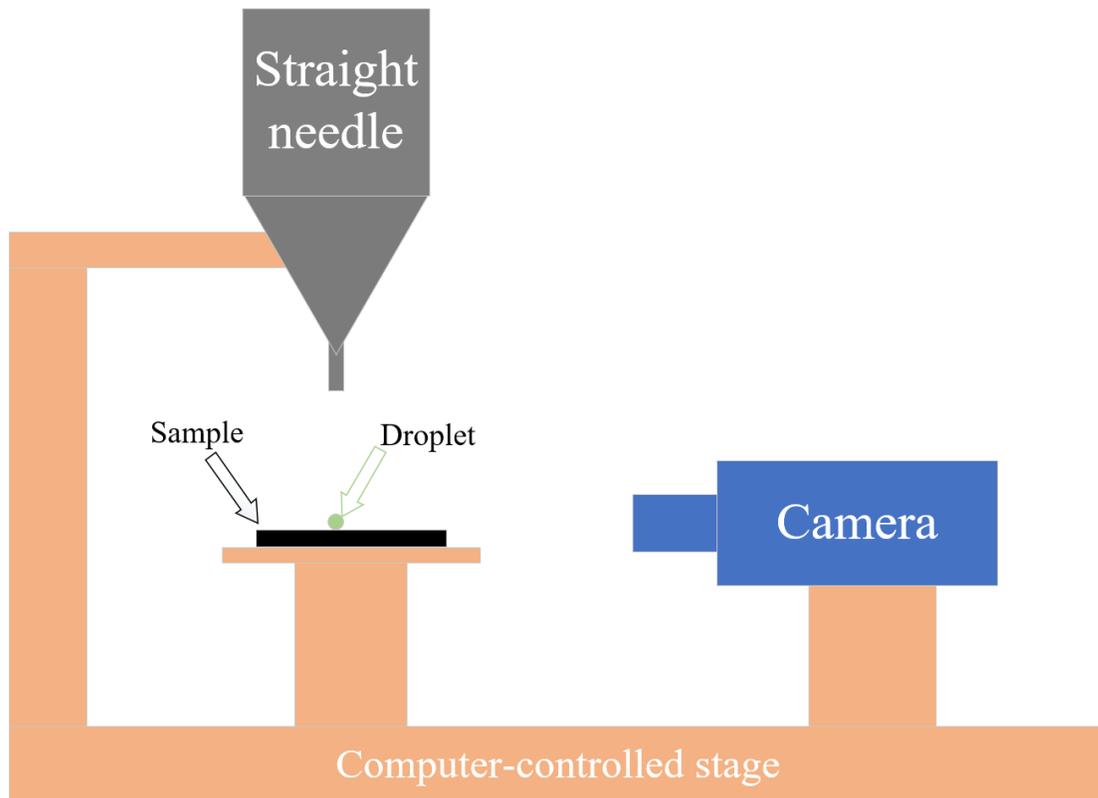
Figure 6. Ramé-hart Goniometer/Tensiometer system.

2.3.   Condensate Freezing Experiment System

A Peltier cooler system was constructed with the following elements: a two-stage Peltier module (Custom Thermoelectric 25412-5L31-07CQQ), a copper water block (Custom Thermoelectric WBA-1.62-0.55-CU-01), and a flat aluminum plate (Custom Thermoelectric CPT-2.25-1.62-0.25-AL). Excess heat from the Peltier cooler was dissipated through a copper cooling block supplied with chilled water at 5 °C supplied by a Lytron circulating chiller (RC006G03BB1C002). The temperature of the flat aluminum plate was controlled with the following elements: a Kapton insulated K-type thermocouple (OMEGA® 5TC-KK-K-20-72); a solid state relay (OMEGA SSRDC100VDC12); a proportional-integral-derivative (PID) controller (OMEGA CNI-16D44); and a voltage

supply (KEPCO JQE 25-10M). The thermocouple was secured and thermally bonded (OMEGA OT-20-1/2) in the compression mounting of the flat aluminum plate. Samples were placed on the flat aluminum plate. Dry nitrogen gas at a velocity of approximately 20 m/s was directed onto the samples to prevent condensation from occurring before the start of data collection. The voltage and current to the Peltier cooler were kept constant at 8 V and 3.85 A, respectively. The PID controller was set to -15 °C. The cycle time for the relay and PID controller was 1 second. The assembled temperature-controlled Peltier cooler system is shown in Figure 7.
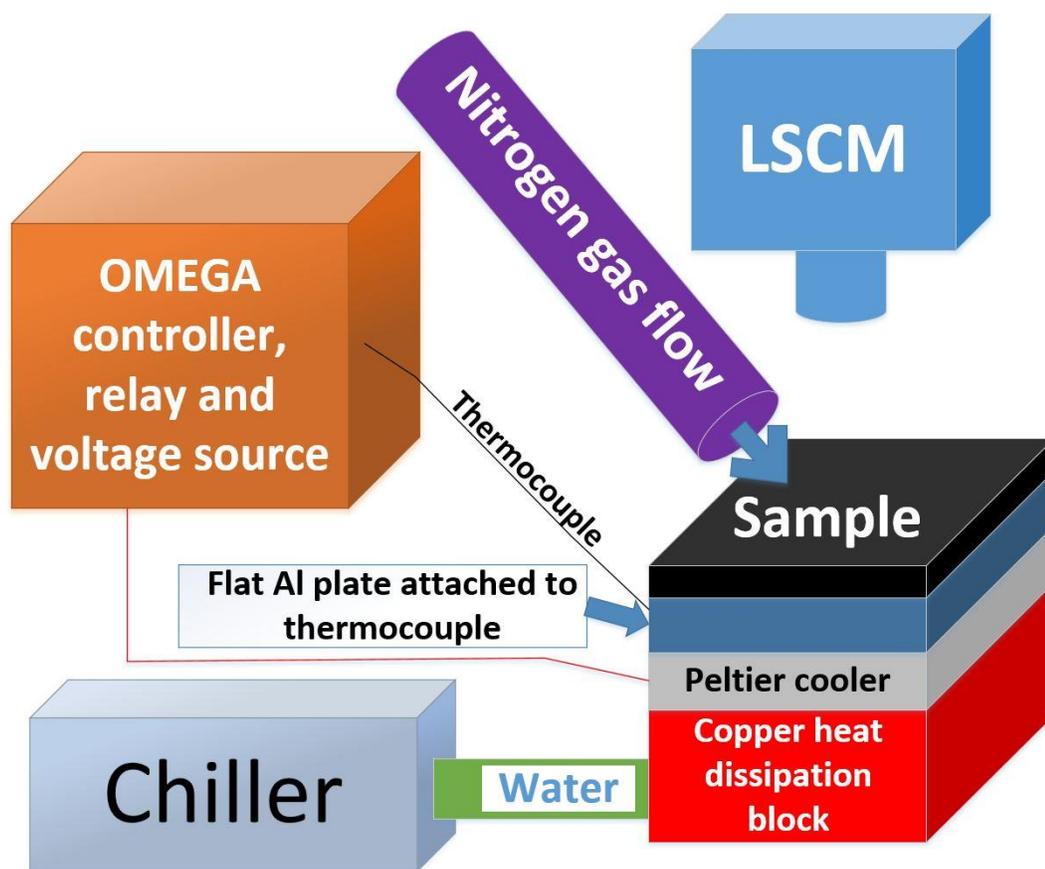
Figure 7. Thermoelectric Peltier cooler system diagram.

With the nitrogen gas flow on and the Peltier on, the samples cooled from room temperature at 22 °C to -2.3 ± 0.2 °C (± as standard deviation). The nitrogen flow was

stopped when data recording was initiated. The temperature of the samples further decreased from -2.3 °C to -15 °C, where it was kept constant by the PID controller switching the relay on and off.

The relative humidity in the room was 25%. Humidity and room temperature were measured using a dual humidity and temperature meter (McMaster-Carr 39175K21). The Peltier cooler system was mounted on the Keyence laser scanning confocal microscope (LSCM) VK-9700 such the visible view was centered on each sample.

The Keyence LSCM provides non-contact, nanometer-level profile, roughness, and surface structure data in this work. The LSCM was used to monitor and record videos of the condensation and subsequent freezing on the samples. The LSCM was used to measure average structure height (R_z). The time required for condensate freezing was defined as when condensates from the atmosphere have frozen (solidified) over the entire surface being monitored by the optical view of the LSCM.

2.4. Self-propelled Jumping Condensates Observation

Self-propelled jumping condensates on FLSP functionalized Al 7075-O Clad surfaces was observed at 8000 fps and recorded using a Photron FASTCAM SA 1.1 high speed camera, with a Nikon Micro-Nikkor AF-S 105 mm f/2.8G ED micro lens and 100 mm extension tubes for increased magnification. The camera was at an incident angle of approximately 45° to the samples. A Dolan-Jenner Fiber-Lite high-intensity illuminator series 180 was used to illuminate the sample. The self-propelled jumping condensates observation system is shown in Figure 8.
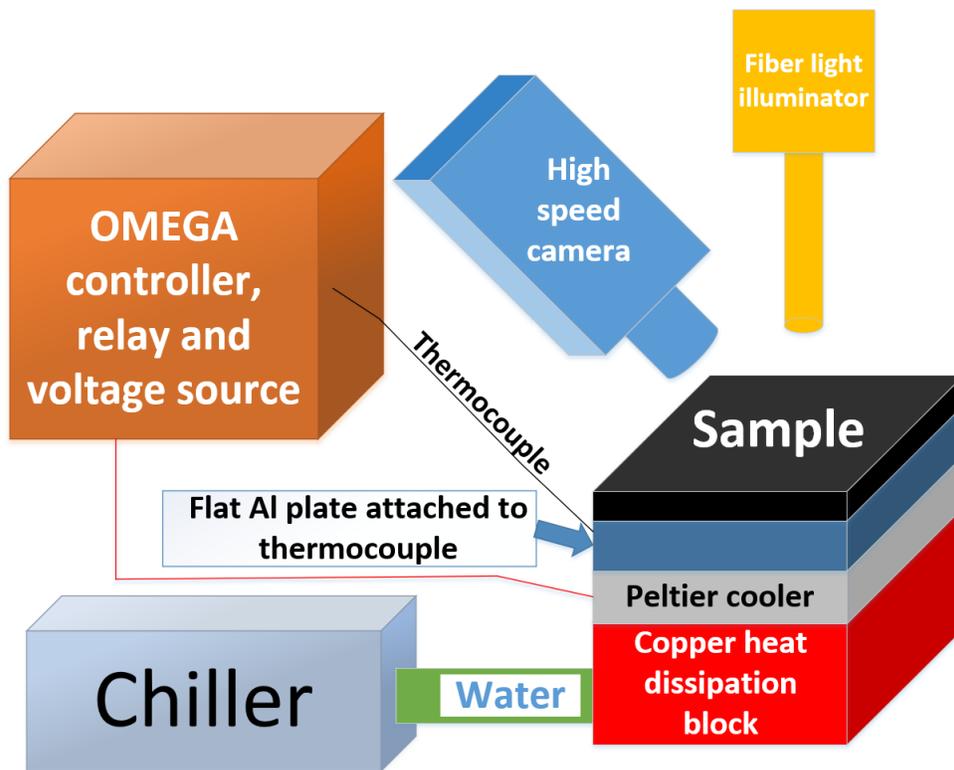
Figure 8. Self-propelled jumping condensates observation system.

The temperature of the samples was dropped from room temperature at 18.5 °C and maintained at -7 °C by the PID controller. The temperature of the samples was controlled with the Peltier cooler system with no nitrogen flow. The relative humidity of the room was 25%.

Chapter 3

Results and Discussion

Laser scanning confocal microscopy 3D view and SEM images of the unprocessed Al 7075-O Clad and two different structure subsets height were created and, small mound structure (SMS) and tall mound structure (TMS), are shown in Figure 9. The surface morphology can be clearly determined by the LSCM 3D view. The structure of the TMS contains more mounds and higher mounds than the SMS. The unprocessed Al 7075-O Clad surface is relatively flat and contains very little structure at this magnification. More mounds and higher mounds in the TMS also indicates that the TMS has the largest surface area when compared to the SMS and an unprocessed surface, which could play an important role in the delay of freezing. Nanoscale particles can be observed on the TMS and SMS by zooming in on the SEM images. By comparing the structures of the SMS and TMS before and after the subsequent freezing experiment, it can be seen that freezing did not change the Morphology and structure.
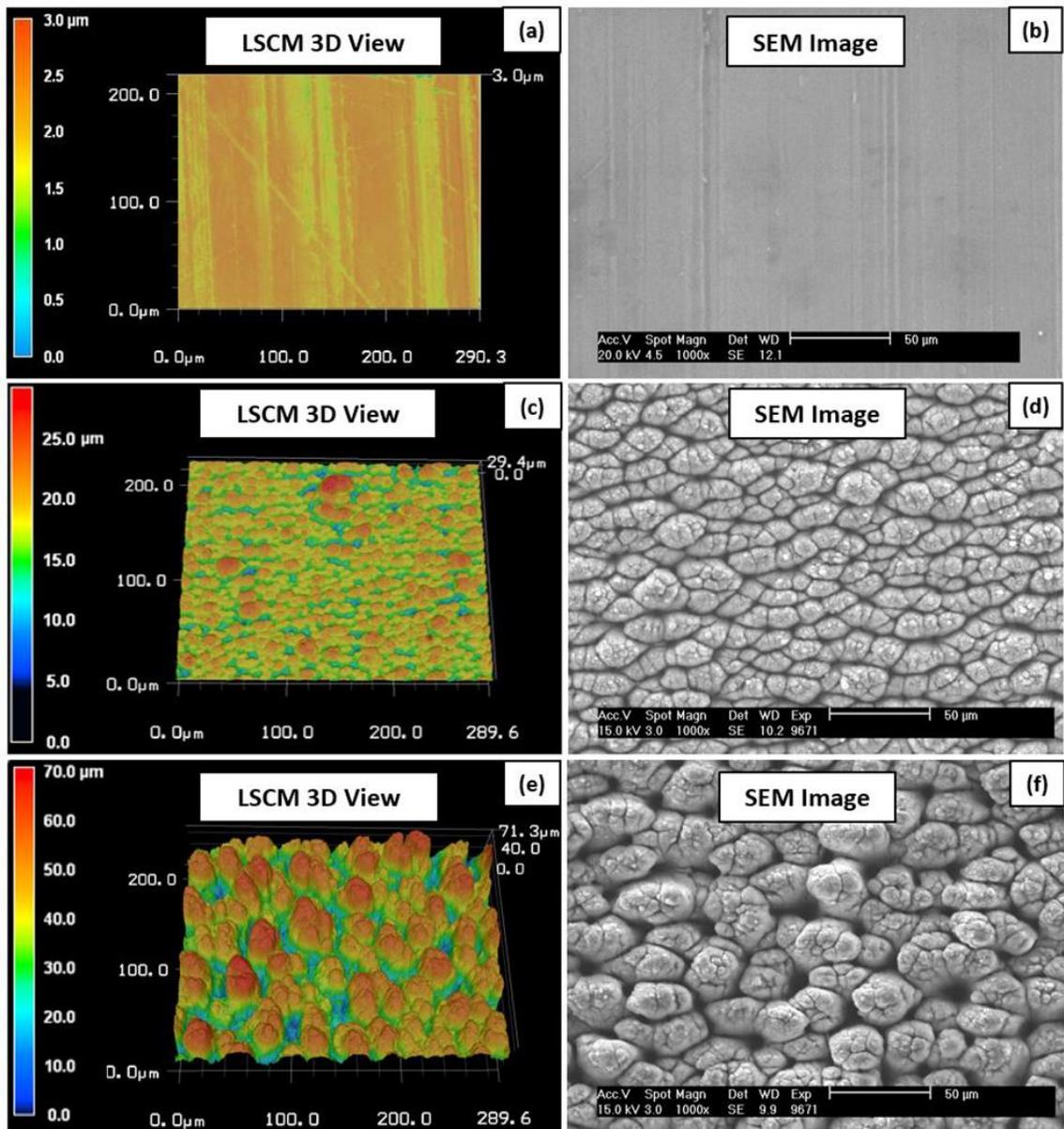
Figure 9. (a) LSCM 3D view of unprocessed Al 7075-O Clad, (b) SEM image of unprocessed Al 7075-O Clad, (c) LSCM 3D view of short mound surface, (d) SEM image of short mound surface, (e) LSCM 3D view of tall mound surface, and (f) SEM image of tall mound surface.

The contact angle measurement figures of unprocessed Al 7075-O Clad and an

FLSP functionalized Al 7075-O Clad surface are shown in Figures 10 (a) and 10 (b). An

optical image of FLSP functionalized Al 7075-O Clad is shown in Figure 10 (c). After

FLSP functionalization, the surfaces were broadband absorbers and appeared black.
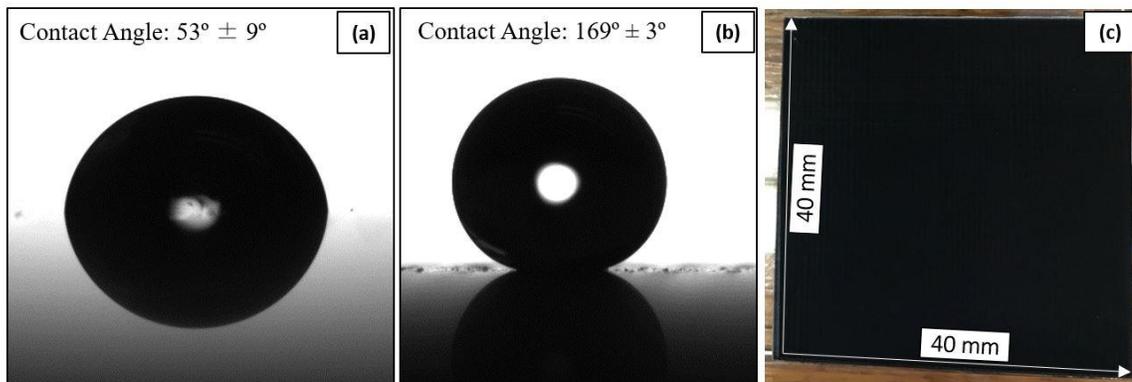
Figure 10. The contact angle measurement figures of (a) unprocessed Al 7075-O Clad and (b) FLSP functionalized Al 7075-O Clad surface. (c) The optical image of FLSP functionalized Al 7075-O Clad.

After removing the nitrogen flow from the samples, each sample followed a similar

cooling rate to -15 °C, as shown in Figure 11. It should be noted that the temperature of the

superhydrophilic surface dropped faster than that of the other samples. The increased rate

of temperature drop is attributed to the film condensation on the superhydrophilic surface

which acts to insulate the surface from the atmosphere, while condensation on the other

surfaces occurs in a dropwise manner.
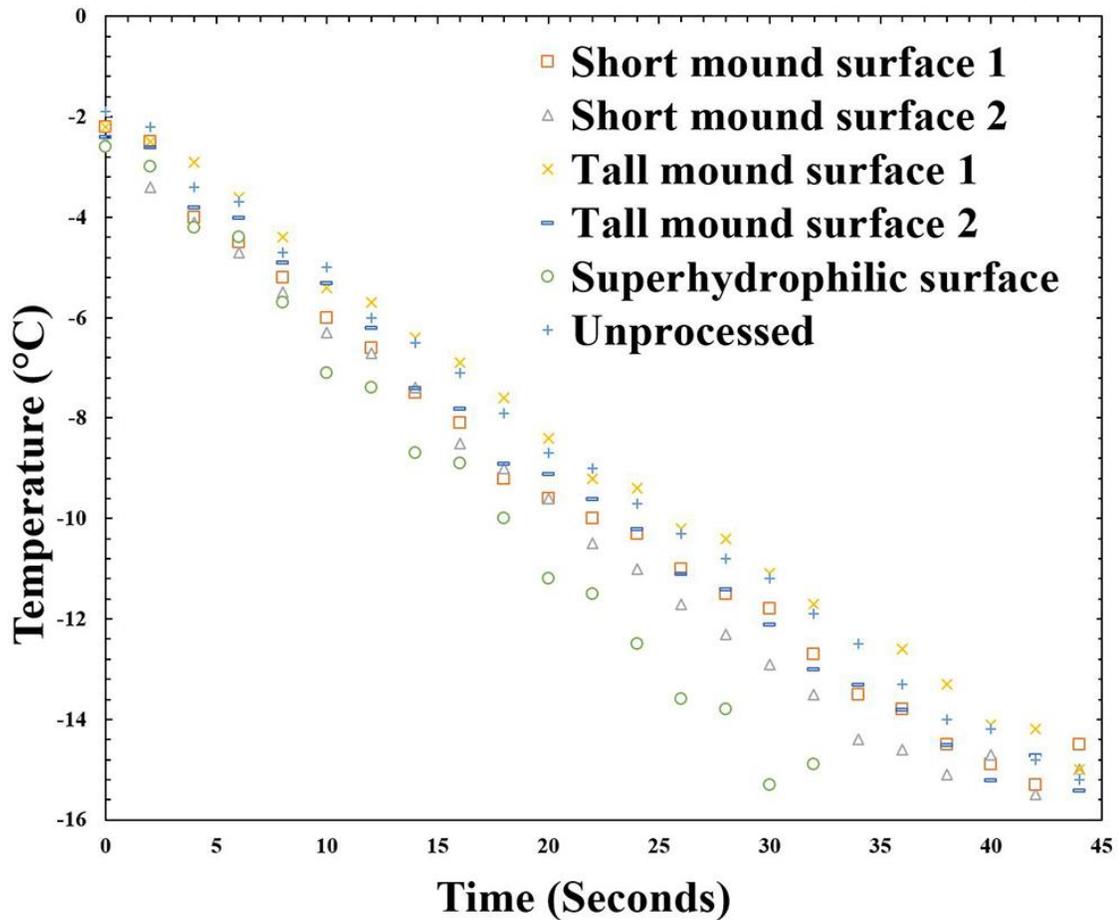
Figure 11. Initial sample cooling from -2.3 °C to -15 °C.

The average structure height, contact angle (CA) before and after the experiment, and the freezing time for each sample are shown in Table 1. The time required to cool the samples to -15 °C is included in the entire surface freezing time. A histogram is shown in Figure 12 to better determine the time requirement for unprocessed Al 7075-O Clad, a superhydrophilic surface, an SMS, and a TMS.

Table 1. Sample surface characteristics, contact angle (CA) before and after the experiment, and condensation and subsequent freezing.

	Average Height R_z (μm)	CA Before Experiment (°)	CA After Experiment (°)	Entire Surface Freezing Time (s)
Unprocessed Al 7075-O Clad	1.2 ± 0.6	53 ± 9	77 ± 2	188
Superhydrophilic surface	55.3 ± 4.4	0	0	41
SMS1	21.2 ± 5.2	168 ± 2	168 ± 4	545
SMS2	16.9 ± 3.0	170 ± 4	168 ± 2	567
Average data of SMS	18.9 ± 4.8	169 ± 2	168 ± 3	556
TMS1	56.4 ± 7.8	168 ± 3	167 ± 2	696
TMS2	47.8 ± 4.3	169 ± 3	166 ± 1	718
Average data of TMS	53.3 ± 7.6	168 ± 3	167 ± 2	707
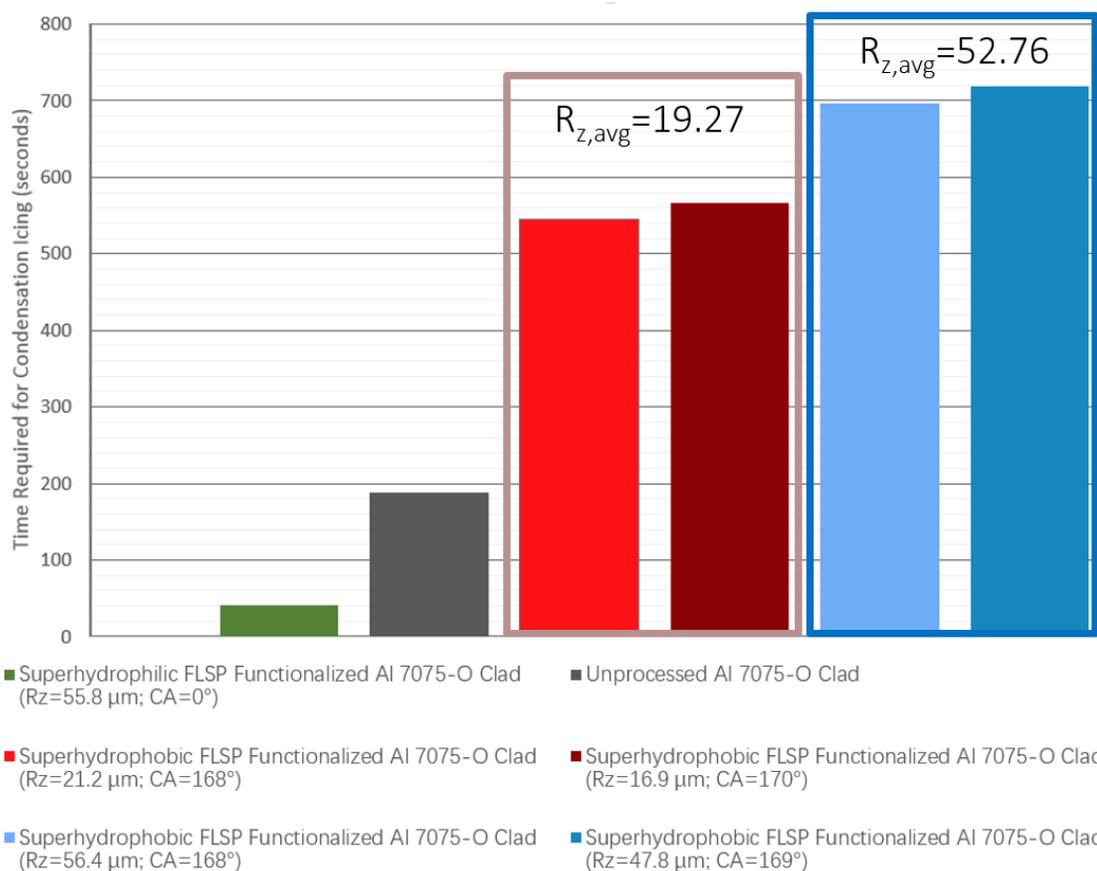
Figure 12. Histogram of the time requirement for unprocessed Al 7075-O Clad,
a superhydrophilic surface, an SMS, and a TMS.

The superhydrophilic sample froze faster (41 seconds) than the unprocessed sample (188 seconds). Freezing of all superhydrophobic surfaces was delayed for at least 357 seconds after the unprocessed surfaces froze. It should be noted that freezing was delayed longer for the sample with a higher CA for each structure subset compared to its respective counterpart. Surface chemistry plays an important role in the delay of condensate freezing on FLSP structures of similar height. For equivalent-sized droplets on superhydrophobic surfaces, the contact area for heat conduction was inversely proportional to the contact

angle of the surface. The impact of CA has been previously shown to delay freezing of condensation on other substrates. [16]

Siloxanes TMS1 and TMS2 both delayed the onset of freezing longer than both SMS1 and SMS2. The contact angle of TMS and SMS are relatively the same. The main difference is the structure height. Therefore, both structure morphology and surface chemistry were important properties in delaying the onset of subsequent freezing. In this work, only two sets of samples with different structure heights were made; and the maximum of the average structure height was around 56.4 µm. The error bars given in Table 1 are thus an average value of the two sample data set. However, by using FLSP, a structure height above 200 µm can be achieved with using other laser parameters not germane to this work.

Still frame images (captured during LSCM optical view) of the progression of condensation and subsequent freezing on all sample subsets are shown in Figure 13.

A comparison of still frame images of the early stage of condensation shows that the superhydrophilic surface condensed a film of water instead of water droplets. Both unprocessed Al 7075-O Clad, SMS, and TMS condense droplets on their surfaces. However, by comparing (d), (g), and (j), the TMS had fewer condensates compared to the SMS and unprocessed Al 7075-O Clad at 39 seconds. In addition, the SMS surface had fewer condensates than unprocessed Al 7075-O Clad at 39 seconds. One hypothetical reason is that the TMS had more surface area than the SMS and unprocessed Al 7075-O Clad, and some condensates cannot be visualized in this image because they are out of focus.

By comparing the still frame images of the coalescence of condensates in (e), (h), and (k), the droplets in the TMS are relatively larger than the SMS and unprocessed Al 7075-O Clad. The surface area could potentially play an important role since there are more small droplets in the TMS area monitored. More small droplets combined to create larger droplets on the TMS surface than on the SMS and unprocessed Al 7075-O Clad surfaces.

Note that as the condensations froze, shown in (c), (f), (i), and (l), the transparency and shape of the condensates were altered. The frozen condensation on the SMS is more opaque than on the TMS indicating that prior to freezing, condensation on the SMS existed at higher supercooling than on the TMS [17], [18]. The transparency change is a result of rapid kinetic freezing of the condensation [19]. According to Criscione et al., "in the absence of any flow the pure diffusive evaporation rate of the supercooled water drop is negligibly small and the heterogeneous nucleation at the solid-liquid interface, corresponding to lower critical energy barrier, initiates freezing" [20]. In a work by Campbell et al., they conclude that water drops freeze at a temperature close to the homogeneous limit on silicon, glass, and mica surfaces [21].
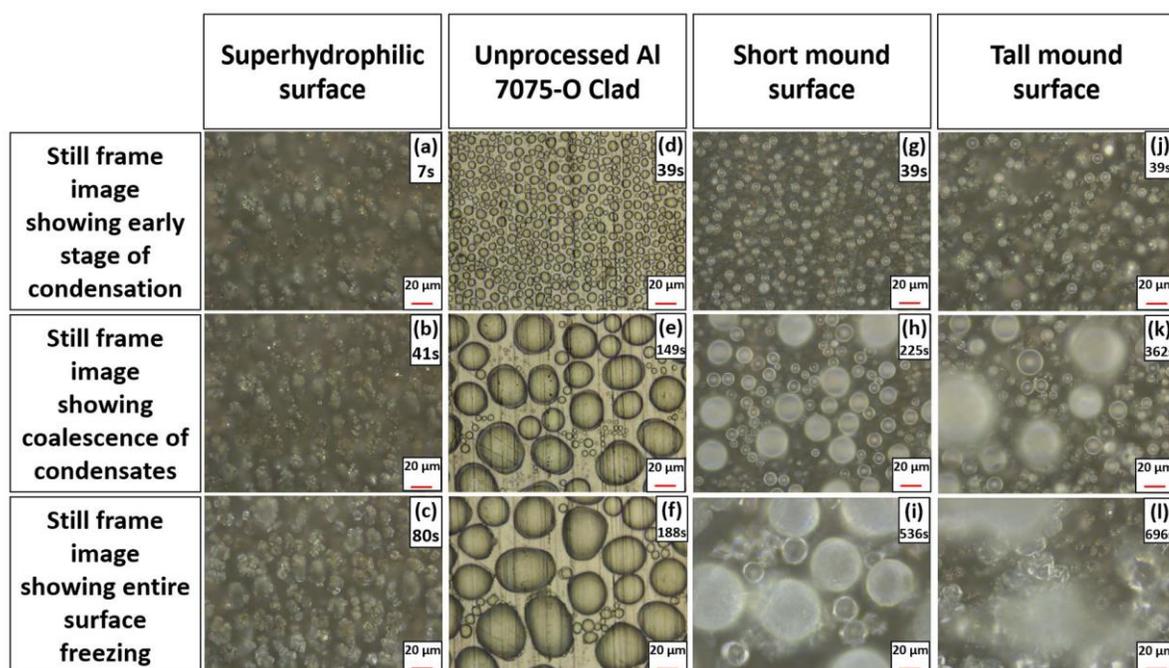
Figure 13. (a), (b), and (c) Condensation and subsequent freezing progression images of a superhydrophilic FLSP functionalized surface. (d), (e), and (f)] Progression images of an unprocessed Al 7075-O Clad surface. (d), (e), and (f) Progression images of SMS. (j), (k), and (l) Progression images of TMS. Videos of the entire surface freezing of each sample are shown in Video 1, Video 2, Video 3, and Video 4.

As shown in Figure 13,water vapor condenses into droplets on the unprocessed surface (d), SMS (g), and TMS (j); and the condensate drops grow [(e), (h), and (k)], coalesce, and eventually freeze [(f), (i), and (l)]. On the superhydrophilic sample, condensate droplets are not easily observed; however, the growth and eventual freezing of a film of ice on the surface was observed (c).

Four videos are helpful to visualize the condensation and its subsequent freezing on each type of surface. All four videos have four quadrants, and descriptions of each quadrant are provided in Table 2. Videos were recorded using a separate video image system from LSCM monitoring screen. The videos were used to determine when the surface was completely frozen. The running clock corresponds to the time when the dry nitrogen flow from the sample was stopped and condensation began. Each quadrant corresponds to each surface. The specific surface/quadrant analyzed is displayed at the

bottom of the video frame. All videos were taken simultaneously although each surface froze over at different time scales, which is highlighted by the videos. Video 1 focuses on a superhydrophilic FLSP functionalized surface. Video 2 focuses on an unprocessed Al 7075-O Clad surface. Video 3 focuses on a superhydrophobic SMS and Video 4 focuses on a superhydrophobic TMS.

Table 2. Explanation of Video 1 (start to 69 seconds), Video 2 (131 to 191 seconds), Video 3 (481 to 549 seconds), and Video 4 (632 to 701 seconds) describing dynamics of the videos.

Quadrant 1: Superhydrophilic FLSP functionalized surface	Quadrant 2: Unprocessed Al 7075-O Clad
Video 1: Condensation and subsequent freezing are hard to observe when viewed at the original speed. However, by comparing frames before 41 seconds and after 41 seconds (35 seconds and 50 seconds), one can recognize the freezing of condensate on the superhydrophilic FLSP functionalized surface. **Videos 2–4:** The surface has already frozen, and a still image of the end of Video 1 is used for better viewing and comparison of characteristics.	**Video 1:** Surface is condensing water. **Video 2:** The surface freezes at 188 seconds. **Video 3–4:** The surface has already frozen, and a still image of the end of Video 2 is used for better viewing and comparison of characteristics.
Quadrant 3: Short mound surface	**Quadrant 4: Tall mound surface**
Video 1-2: Surface is condensing water. **Video 3:** The surface is freezing at 545 seconds. **Video 4:** The surface has already frozen, and a still image of the end of Video 3 is used for better viewing and comparison of characteristics.	**Videos 1-3:** Surface is condensing water. **Video 4:** The surface is freezing at 696 seconds.

The stages of condensation have been reported previously [22]–[24]. In the work by Enright et al., early stages of condensation have been shown on a self-assembled hydrophobic monolayer rely on the spontaneous formation of a thin molecular film (~1 nm) on the condensing surface. The images of this work is recorded by an environmental

transmission electron microscopy (ETEM) [24]. The constant base droplet growth on a hydrophobic surface is shown in Figure 14.
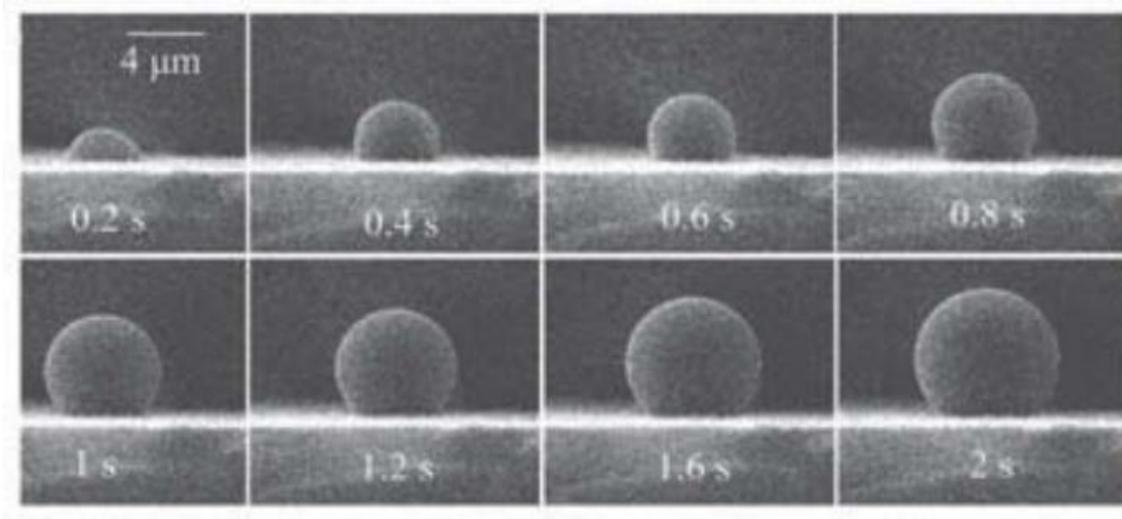
Figure 14. Constant base droplet growth on a hydrophobic surface. [24]

Time frames of condensation is shown in Figure 14. At 0.2 s, although the surface is hydrophobic, the contact angle of the micron-scale water droplet is small. From initial time 0 s to 0.6 s, the contact angle of the micron-scale water droplet is growing with the growth of the droplets size. After the contact angle of the micron-scale water droplet reaches a limit, in this case, the time between 0.6 s to 0.8 s. After 0.8 s the droplet grows with the relative same contact angle. This work by Enright et al., can be applied to the FLSP surfaces. Although the contact angle measured by ramé-hart Goniometer/Tensiometer system is above 150°, at the initial stage of condensation, the droplets size increases while the contact angle of micro-scale water droplets increases. After the contact angle of micro-scale water droplets reaches a limit, the droplets size increases with the relatively same contact angle in SMS and TMS.

According to Zheng et al., ESEM is used in situ investigation on dynamic suspending of microdroplet on lotus leaf and gradient of wettable mcro-and nanostructure from water condensation [23]. There are three processes for illustration of microdroplet suspension are shown in Figure 15. Process 1 is a small microdroplet in the valley of papillae. Process 2 is that microdroplet is deformed, with the contact angle θ_d of down edge larger than the contact angle θ_u of upper edge. The unbalanced surface tension drives the microdroplet directionally moves toward the top of papillae. Process 3 is that microdroplet is ultimately suspended on the tops of the papillae. The arrow indicates the direction of microdroplet movement.
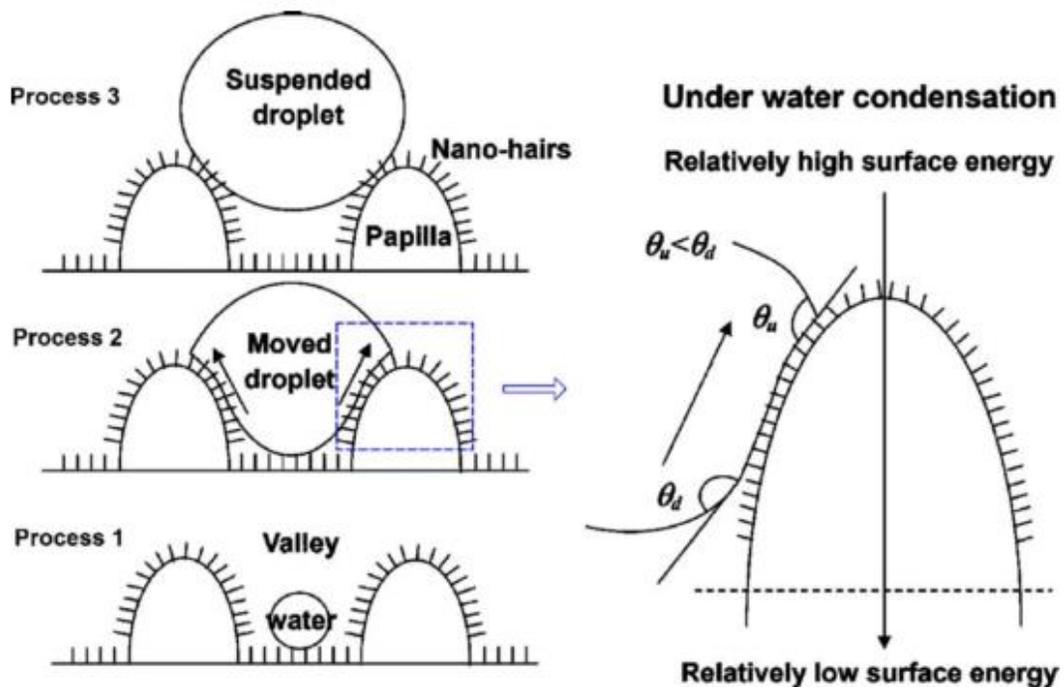
Figure 15. Processes of illustration of microdroplet suspension. [23]

By applying the work from Zheng et al., condensation happens first under the "valley" firstly. As the water droplets grow, finally the droplets will be suspended on the

mounds [23]. The still frame images of the TMS, visualized by the LSCM, are shown in Figure 16.
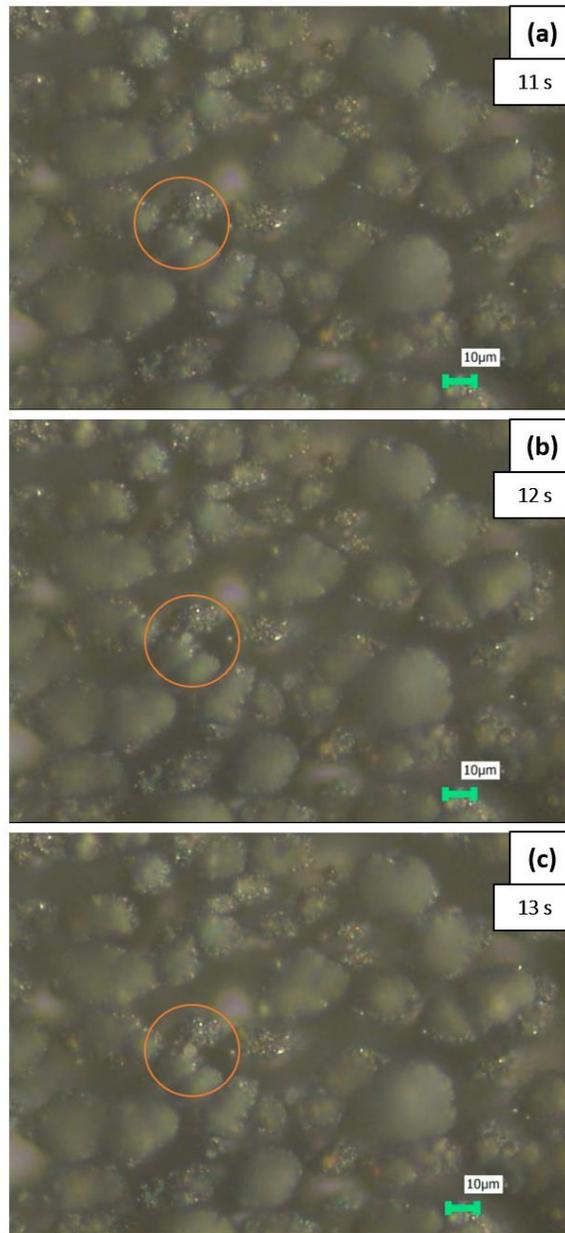
Figure 16. Still frame images of the first condensate is monitored at (b) 12 s on TMS1.

In Figure 16, the first condensate is monitored at 12 s on TMS 1. Before 12 s, condensates are too small to be monitored. According to Zheng et al., condensation happens first in the "valley" in both SMS and TMS [23]. The first droplets is monitored at

between the mounds and suspended on the "valley", which proves that condensation happens first in the "valley" starting with micron-scale droplets that can not be monitored by LSCM.

Condensates on the TMS and SMS exhibit self-propelled jumping away from the FLSP surface. Although self-propelled condensate jumping has been shown on other superhydrophobic surfaces [14], this is the first time self-propelled jumping on FLSP surfaces has been reported in the literature. A still image sequence of self-propelled condensate jumping on TMS1 is shown in Figure 17.
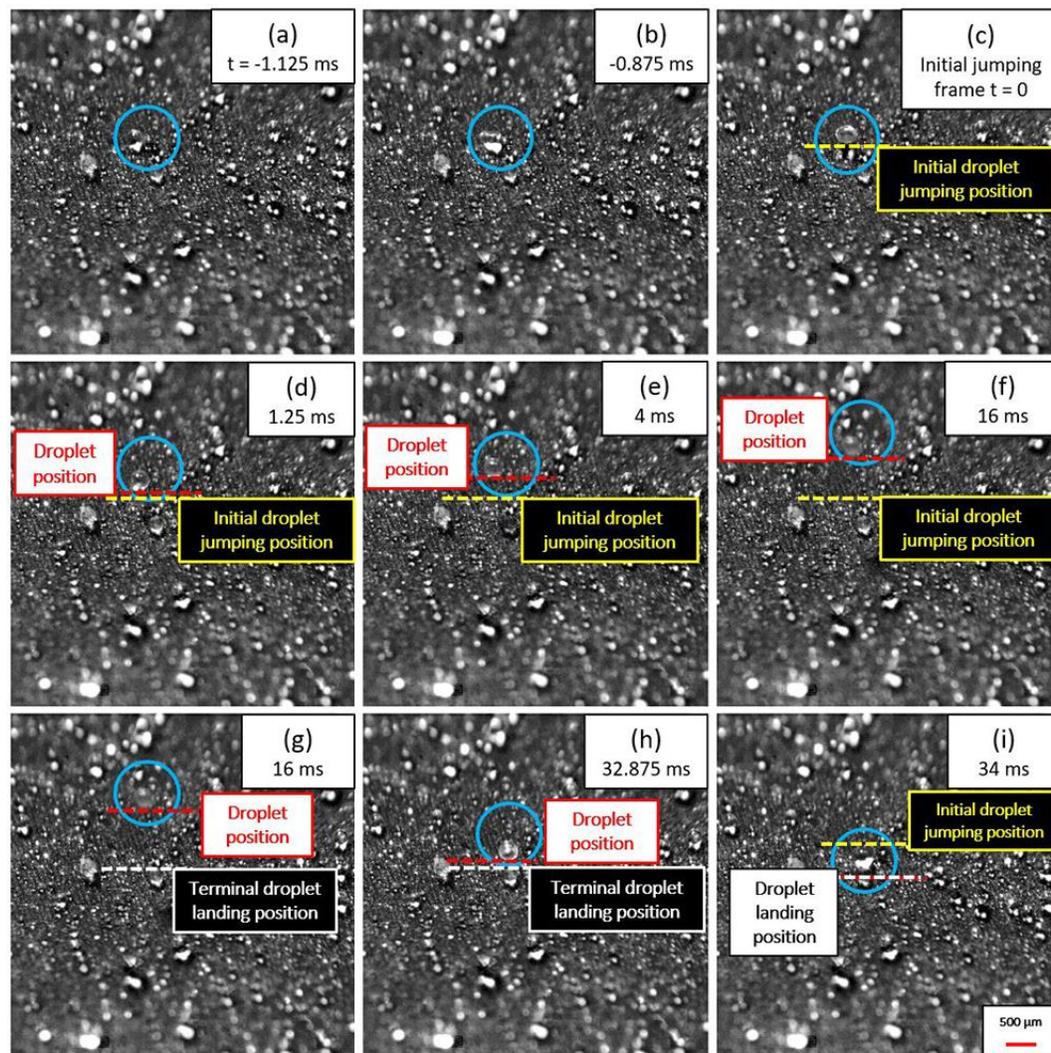
Figure 17. (a), (b), and(c) Still frame images of two condensate drops combining. (d), (e), and (f) Jumping off the surface. (g), (h), and (i) Falling due to gravity. The video of this progression is shown in Video 5.

Still frame images of the SMS and TMS, visualized by the LSCM, are shown in Figure 18. From (a) to (b) in one second, droplets combined and jumped off the SMS surface. From (c) to (d) in one second, droplets combined and jumped off the TMS surface. During the condensation and subsequent freezing process, self-propelled condensates jumping happened on both the SMS and TMS. However, in the monitored area, the self-propelled condensates jumping on the TMS removed a larger area of droplets than the

SMS. This result also indicates that TMS has better self-clean and anti-icing properties than SMS.
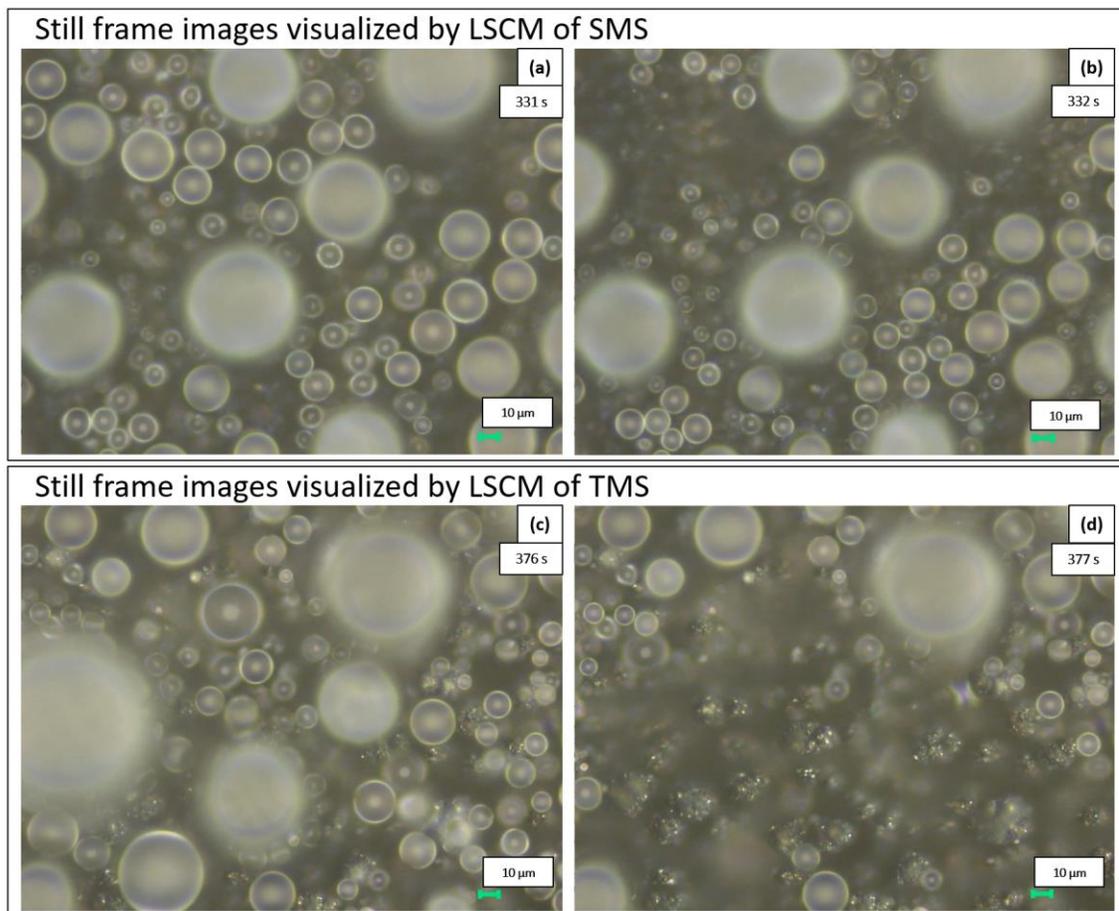
Figure 18. Still frame images of SMS (a) and (b), and TMS (c) and (d) as visualized by the LSCM.

Self-propelled condensate jumping is important for delaying the time required for freezing of condensation, as it acts to remove droplets which can initiate freezing on the surface. Self-propelled condensate jumping is strongly influenced by the wettability. Wisdom et al. demonstrated a unique self-cleaning mechanism whereby the contaminated superhydrophobic surface is exposed to condensing water vapor; and the contaminants are autonomously removed by the self-propelled jumping motion of the resulting liquid condensate, which partially covers or fully encloses the contaminating particles [14]. The higher the contact angle, the lower the energy required to detach a spherical particle from

a flat interface. "The energy required to detach a spherical particle from a flat interface is proportional to $(1 - |\cos\theta|)^2$, where θ is the contact angle of water on the particle." [25].

Wisdom et al. demonstrated a floating removal process in Figure 19: "A 50- µm-diameter glass particle was initially floated inside a condensate drop. When this drop coalesced with a neighboring drop, the capillary-inertial oscillation of the merged drop interacted with the superhydrophobic surface, resulting in an out-of-plane jumping drop that carried away the floated particle." [14]
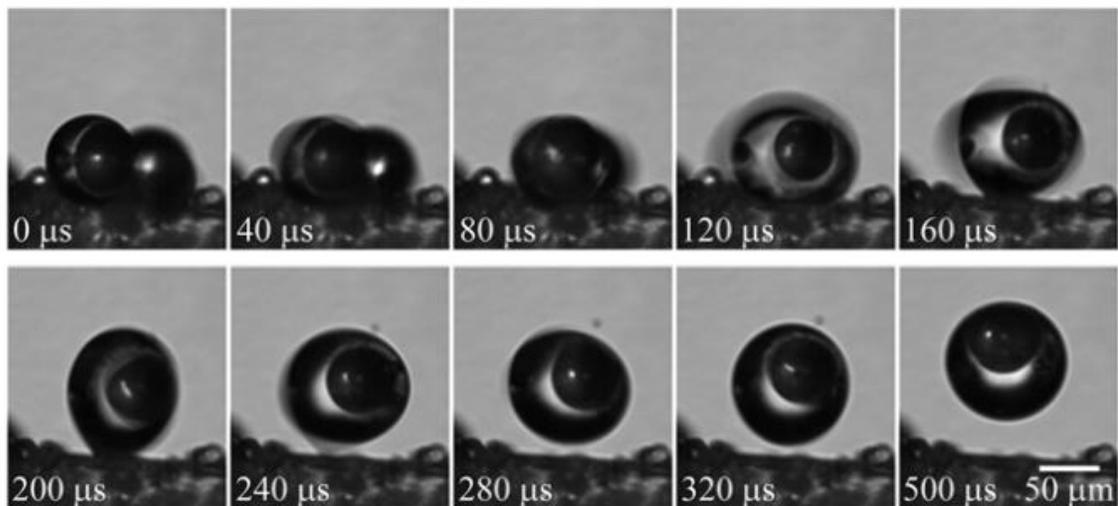

Figure 19. Floating removal process. [14]

If the sample can be tilted to a certain angle, the jumping droplets could not bounce back to the surface. The self-cleaning and anti-icing property could be enhanced. An example system diagram is shown in Figure 20.
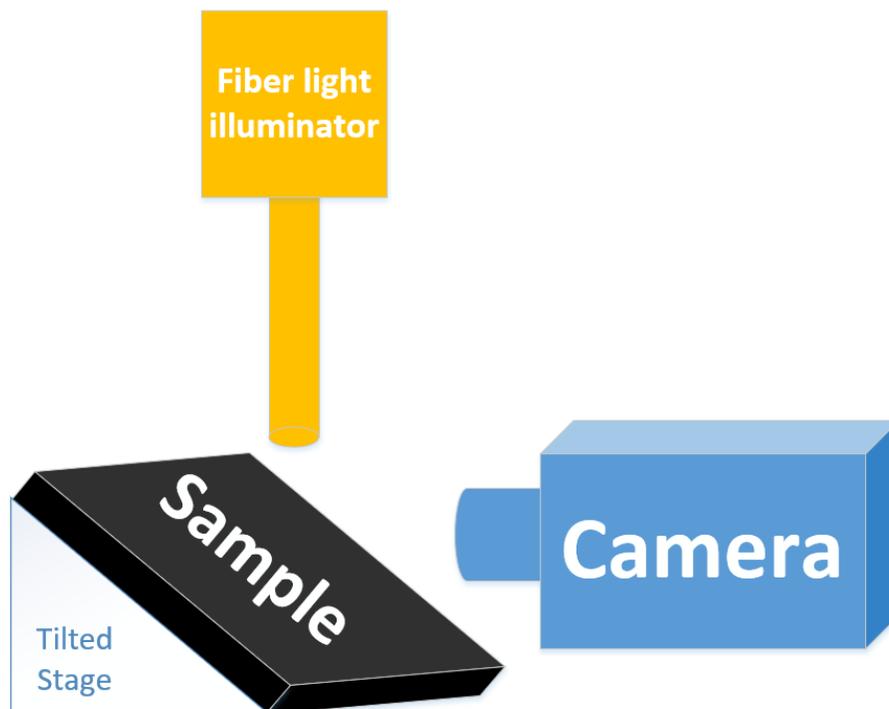
Figure 20. Diagram of a tilted condensation and subsequent freezing observation system.

Chapter 4

Future Work, Summary, and Conclusions

4.1. Future Work

The next step in this work will be to explore different height structures to maximize the delay of subsequent freezing, and the eventual goal is to prevent condensation icing from even occurring. Higher structure height samples can be made and used to verify if the higher structure height would delay subsequent freezing for a longer period of time than obtained in this work. The affect in different relative humidity during the condensation and subsequent freezing could be achieved using a portable microscope visualized in an environmental chamber. The tilted surface can be tested for the longer condensation and subsequent delay time since the self-propelled jumping droplets could jump off the surface instead of bouncing back to the surface. The future work will also include exploration of large-scale condensation removal prior to freezing by optimizing self-propelled droplet jumping.

In addition, different metal materials can be investigated for another anti-icing study. An anti-icing study of stainless steel and copper would be desirable for many other applications.

4.2. Summary and Conclusions

In this work, an FLSP functionalized Al 7075-O Clad superhydrophilic surface, a TMS, and an SMS were processed. The freezing time of the unprocessed Al 7075-O Clad was 188 seconds. The freezing time of the superhydrophilic FLSP functionalized Al 7075-O Clad surface was 41 seconds. The freezing time of SMS1 and SMS2 was 556 ± 11

seconds. The freezing time of TMS1 and TMS2 was 707 ± 11 seconds. This work provided insight to the effect that surface modification has on the freezing time of FLSP surfaces. It is important to point out the FLSP surfaces are self-organized and have non-symmetric features. Self-propelled condensate jumping on FLSP structures is reported for the first time to our knowledge in the literature.

References

[1]   M. Lee, C. Yim, and S. Jeon, "Communication: Anti-icing characteristics of superhydrophobic surfaces investigated by quartz crystal microresonators," *J. Chem. Phys.*, vol. 142, no. 4, 2015.

[2]   S. Farhadi, M. Farzaneh, and S. A. Kulinich, "Anti-icing performance of superhydrophobic surfaces," *Appl. Surf. Sci.*, vol. 257, no. 14, pp. 6264–6269, 2011.

[3]   S. A. Kulinich and M. Farzaneh, "Ice adhesion on super-hydrophobic surfaces," *Appl. Surf. Sci.*, vol. 255, no. 18, pp. 8153–8157, 2009.

[4]   L. Makkonen, "Ice Adhesion —Theory, Measurements and Countermeasures," *J. Adhes. Sci. Technol.*, vol. 26, no. 4–5, pp. 413–445, 2012.

[5]   L. Makkonen, "Surface Melting of Ice," *J. Phys. Chem. B*, vol. 101, no. 32, pp. 6196–6200, 1997.

[6]   S. Jung, M. Dorrestijn, D. Raps, A. Das, C. M. Megaridis, and D. Poulikakos, "Are superhydrophobic surfaces best for icephobicity?," *Langmuir*, vol. 27, no. 6, pp. 3059–3066, 2011.

[7]   Q. Hao, Y. Pang, Y. Zhao, J. Zhang, J. Feng, and S. Yao, "Mechanism of delayed frost growth on superhydrophobic surfaces with jumping condensates: More than interdrop freezing," *Langmuir*, vol. 30, no. 51, pp. 15416–15422, 2014.

[8]   C. Antonini, M. Innocenti, T. Horn, M. Marengo, and A. Amirfazli, "Understanding the effect of superhydrophobic coatings on energy reduction in

anti-icing systems," *Cold Reg. Sci. Technol.*, vol. 67, no. 1–2, pp. 58–67, 2011.

[9]   J. B. Boreyko and C. P. Collier, "Delayed frost growth on jumping-drop
        superhydrophobic surfaces," *ACS Nano*, vol. 7, no. 2, pp. 1618–1627, 2013.

[10]   A. S. Van Dyke, D. Collard, M. M. Derby, and A. R. Betz, "Droplet coalescence
        and freezing on hydrophilic, hydrophobic, and biphilic surfaces," *Appl. Phys. Lett.*,
        vol. 107, no. 14, pp. 1–5, 2015.

[11]   J. Li, Y. Zhao, J. Hu, and L. Shu, "Anti-icing Performance of a Superhydrophobic
        PDMS / Modified Nano-silica Hybrid Coating for Insulators," *J. Adhes. Sci.
        Technol.*, vol. 26, no. May, pp. 665–679, 2012.

[12]   C. a Zuhlke, T. P. Anderson, and D. R. Alexander, "Formation of multiscale
        surface structures on nickel via above surface growth and below surface growth
        mechanisms using femtosecond laser pulses," *Opt. Express*, vol. 21, no. 7, pp.
        8460–8473, 2013.

[13]   X. Qu *et al.*, "Self-propelled sweeping removal of dropwise condensate," *Appl.
        Phys. Lett.*, vol. 106, no. 22, pp. 1–5, 2015.

[14]   K. M. Wisdom *et al.*, "Self-cleaning of superhydrophobic surfaces by self-
        propelled jumping condensate.," *Proc. Natl. Acad. Sci. U. S. A.*, vol. 116, no. 20,
        pp. 7992–7, 2013.

[15]   C. a. Zuhlke, T. P. Anderson, and D. R. Alexander, "Comparison of the structural
        and chemical composition of two unique micro/nanostructures produced by
        femtosecond laser interactions on nickel," *Appl. Phys. Lett.*, vol. 103, no. 12, pp.

14–19, 2013.

[16] P. Tourkine, M. Le Merrer, and D. Quéré, "Delayed freezing on water repellent materials," *Langmuir*, vol. 25, no. 13, pp. 7214–7216, 2009.

[17] M. Schremb and C. Tropea, "Solidification of supercooled water in the vicinity of a solid wall," *Phys. Rev. E - Stat. Nonlinear, Soft Matter Phys.*, vol. 94, no. 5, pp. 2–7, 2016.

[18] S. Jung, M. K. Tiwari, and D. Poulikakos, "Frost halos from supercooled water droplets.," *Proc. Natl. Acad. Sci. U. S. A.*, vol. 109, no. 40, pp. 16073–8, 2012.

[19] L. Oberli, D. Caruso, C. Hall, M. Fabretto, P. J. Murphy, and D. Evans, "Condensation and freezing of droplets on superhydrophobic surfaces," *Adv. Colloid Interface Sci.*, vol. 210, pp. 47–57, 2014.

[20] A. Criscione, I. V. Roisman, S. Jakirlić, and C. Tropea, "Towards modelling of initial and final stages of supercooled water solidification," *Int. J. Therm. Sci.*, vol. 92, pp. 150–161, 2015.

[21] J. M. Campbell, F. C. Meldrum, and H. K. Christenson, "Is ice nucleation from supercooled water insensitive to surface roughness?," *J. Phys. Chem. C*, vol. 119, no. 2, pp. 1164–1169, 2015.

[22] J. Zhu, Y. Luo, J. Tian, J. Li, and X. Gao, "Clustered Ribbed-Nanoneedle Structured Copper Surfaces with High-Efficiency Dropwise Condensation Heat Transfer Performance," *ACS Appl. Mater. Interfaces*, vol. 7, no. 20, pp. 10660–10665, 2015.

[23]   Y. Zheng, D. Han, J. Zhai, and L. Jiang, "In situ investigation on dynamic suspending of microdroplet on lotus leaf and gradient of wettable micro- and nanostructure from water condensation," *Appl. Phys. Lett.*, vol. 92, no. 8, 2008.

[24]   R. Enright, N. Miljkovic, J. L. Alvarado, K. Kim, and J. W. Rose, "Dropwise condensation on micro-and nanostructured surfaces," *Nanoscale Microscale Thermophys. Eng.*, vol. 18, no. 3, pp. 223–250, 2014.

[25]   B. P. Binks and T. S. Horozov, *Colloidal Particles at Liquid Interfaces*. Cambridge University Press, 2006, 2006.